**Article:**
Wang, J., Han, B., Chen, Z. et al. (3 more authors) (Cover date: 15 August 2023) Study on tribological oxide mechanism of CoCrFeNiMo high entropy alloy. Wear, 526-527. 204907. ISSN 0043-1648

https://doi.org/10.1016/j.wear.2023.204907

# Study on tribological oxide mechanism of CoCrFeNiMo high entropy alloy

Jialin Wang[a,b], Bin Han[a]*, Zubin Chen[a], Chunyang Hu[a], Qi Zhang[a], Chun Wang[b]

[a]: School of Materials Science and Engineering, China University of Petroleum (East China), Qingdao, 266580, China

[b]: Institute of Functional Surface, School of Mechanical Engineering, University of Leeds, LS2 9JT, United Kingdom

*Corresponding author: Bin Han, E-mail: hanbin@upc.edu.cn

Abstract: The oxide film can improve the tribological properties of high entropy alloy, but its formation needs further study. In this work, the tribological oxide mechanism of CoCrFeNiMo high entropy alloys was investigated by means of experiments and finite element simulation. Simulation results reveal that the formation and destruction of oxide film are related to contact stress, von Mises stress and tensile stress. The contact stress destroys the passivation film of CoCrFeNiMo high entropy alloy. Then von Mises stress causes plastic deformation on the surface to form oxide films. Finally, tensile stress causes these oxide films to crack. These results were confirmed by the experiment. When CoCrFeNiMo rubs with $ZrO_2$, the increase of load can make the CoCrFeNiMo surface prone to plastic deformation, forming more oxide films. However, when it sildes against stainless steel no oxide film is formed on the surface of CoCrFeNiMo because there is no plastic deformation. Cracks in the oxide film perpendicular to the tensile stress were also observed on the surface, proving the destruction of periodic tensile stress.

**Keywords**: Tribological oxide mechanism, High-entropy alloy, Water lubrication, Finite element modelling

## 1 Introduction

As a new type of alloy material, High entropy alloy (HEA) usually contain five or more elements, which make them have high-entropy effect, lattice distortion effect, slow diffusion effect and cocktail effect[1, 2]. The high-entropy effect and the cocktail effect make the corrosion resistance of HEA superior to nickel-based alloys or stainless steels[3, 4]. In fact, the passivation film formed by Cr, Ni, Mo in the high-entropy alloy ensures its excellent corrosion resistance[5-7]. A metallurgically bonded HEA coatings

on steel surfaces can be prepared by laser cladding. Owing to the large cooling rate and low heat input of the laser cladding, usually, the coating with fine microstructure and excellent mechanical properties can be obtained[8-10], which can significantly increase the performance and service life of the equipment and reduce manufacturing costs[11]. Therefore, HEA coatings are considered as a promising engineering material candidate. At present, there are many studies on the tribological properties of HEA coating owing to its excellent wear resistance and corrosion resistance[12-15]. Despite the protection of passive film, oxide film will still form on the HEA surface, which can significantly affect the tribological properties of HEA[16-18]. For this reason, it is very meaningful to study the tribological oxidation mechanism of high entropy alloys. For the formation of oxide film, researchers mainly explore it through experimental methods[19-22]. The related research showed that the oxide film formed during sliding test is caused by plastic deformation[19, 23-25]. For example, You et al.[26] proved that the oxide films formed on the wear scar of $Ti_xVNbTaW_y$ at 600 ℃ is caused by plastic deformation and these oxide films improved the tribological property of the HEA coatings. In addition to high temperature, high load can also make oxide film from on the HEA coating surface. Deng et al.[25] demonstrated that the main wear mechanisms of $CoCrFeNiMo_{0.2}$ are oxidation and delamination under high loads. In fact, the surface stress, plastic deformation and the formation of oxide film are related[27, 28]. Different stresses have different effects on the formation and destruction of oxide film. To further study the tribological oxidation mechanism of high entropy alloys, the stress distribution on the surface should be analysed during friction. However, there is no relevant research so far.

In this paper, the tribological oxidation behavior of CoCrFeNiMo coating was investigated through the sliding test between CoCrFeNiMo coating and $ZrO_2$/ stainless steel. Then, the stress distribution on the surface of CoCrFeNiMo during sliding test is analyzed by finite element method. The tribological oxidation mechanism of CoCrFeNiMo high entropy alloy was explored by combining experiments and simulations.

## 2 Experimental materials and method

### 2.1 Preparation of CoCrFeNiMo coatings

The CoCrFeNiMo coatings preparation process is shown Figure 1. CoCrFeNi atomized powder mixed with Mo powder were used as preset CoCrFeNiMo powder in this experiment. Laser cladding adopted YSL-6000 IPG fibre laser under the protection of Ar. Cladding parameters were listed in Table 1. The sample was then cut into small pieces (10×20×3 $mm^3$) as shown in Figure 1 (b). The initial thickness of the coating is 1 mm, and the top will be worn off by about 0.3mm during manufacturing operation. After rough grinding, fine grinding and polishing, the surface roughness of CoCrFeNiMo HEA coating is Ra=0.4 μm and the hardness of the CoCrFeNiMo coating surface is 398 HV tested by the Vickers hardness tester. Before sliding test, the polished sample was in acetone for 15 minutes to remove any impurities.

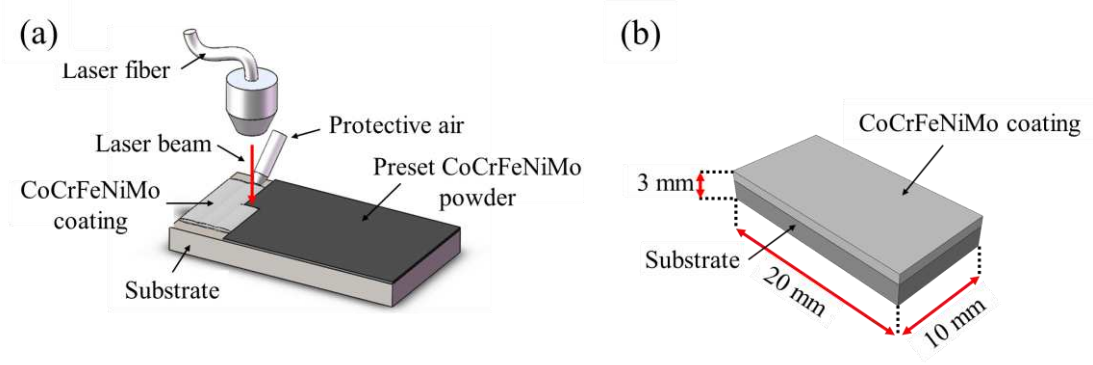


Figure 1 Preparation process of CoCrFeNiMo coating, a) laser cladding diagram, b) the developed CoCrFeNiMo coating diagram

Table 1 Parameters of laser cladding

| Scanning speed | Laser power | Overlapping ratio | Preset powder thickness | Spot size |
|---|---|---|---|---|
| 300 mm/min | 2700 W | 30% | 1 mm | 10 mm × 1 mm |

### 2.2 Friction and wear test

All sliding tests were carried out on MFT-EC4000 reciprocating tribometer, where a 6 mm diameter ball was loaded against the coated sample. The materials of the ball are $ZrO_2$ and 304 stainless steel (SS). The hardness of $ZrO_2$ and 304 stainless steel are 1200

HV and 210 HV respectively. The yield strength of stainless steel is lower than that of CoCrFeNiMo coating. Therefore, when the micro convexes contact, the stainless-steel balls yield first, which reduces plastic deformation of CoCrFeNiMo coating. However, when $ZrO_2$ contacts with CoCrFeNiMo, CoCrFeNiMo is more prone to plastic deformation. In this way, the effect of plastic deformation on the formation of oxide film can be studied. The ball and CoCrFeNiMo coating were completely immersed in distilled water during the sliding test. Distilled water can remove the debris from the wear marks. The sliding distance was 5 *mm*, the sliding frequency was 2 *Hz*, the load used was 2-10 *N*, the test time was 1800 *s*, the average sliding velocity was 20 *mm / s*.

2.3 Material characterization

X-Pert PRO MPD X-Ray Diffraction (XRD) was used to determine the phase constitution of CoCrFeNiMo, scanning from 20°-100°, Cu target, scanning rate of 2° $min^{-1}$. Zeta-200 3D surface profiler was used to measure the depth and width of the wear scar. Gamry 1010T electrochemical workstation with a conventional three-electrode cell system is used to test potentiodynamic polarization curves, and 3.5 wt% NaCl solution was used as the electrolyte. Pt plate (20mm×20mm) as the counter electrode, and a saturated calomel electrode (SCE) as the reference electrode. The test surface (15mm×15mm) was exposed after the sample was sealed. The potentiodynamic polarization curves of the samples were measured at a scanning rate of 1 mV/s. The electrochemical analysis software Gramy ESA410 was used to calculate $E_{corr}$ and $J_{corr}$. $23CrNi_3Mo$ carburized steel is used in various equipment as a common wear-resistant material and its chemical composition as shown in Table 2, so it was selected as the comparison material. The passive film compositions were measured by utilizing Thermo Fisher ESCALAB XI+ X-ray photoelectron spectroscopy (XPS) equipped with Al Kα radiation. The binding energy is adjusted though the standard $C_{1s}$ at peak of 284.8 eV. The morphology and the chemical composition of the CoCrFeNiMo coating were studied by Scanning Electron Microscopy (SEM, JEM-7200F) equipped with EDS (X-MAX50). Raman spectroscopy with a 488 nm laser was used to characterize the oxide after the wear test, exposing for 10 *s* with 30% laser power.

Table 2 Chemical Composition of 23CrNi3Mo in wt%

| Element | C | Si | Mn | Cr | Ni | Mo | S |
|---|---|---|---|---|---|---|---|
| Content | 0.25 | 0.2565 | 0.6455 | 1.272 | 2.9285 | 0.246 | 0.003 |

2.4 Stress distribution simulation in coated surfaces

Finite element analysis (FEA) of stress distribution was conducted using ABAQUS to build the sliding test model. The schematic diagram of the sliding test simulation is shown in Figure 2. In order to improve the accuracy of simulation, only some parts are selected to simulate in this work, which are shown in Figure 2(b)[29]. The entire model is divided into 70848 hexahedral elements by using the C3D8R element (After grid independence analysis, the number of grids is doubled, and the error between the results is less than 1%). The material properties are shown in Table 3 and the $ZrO_2$ ball is considered a discrete rigid body[30]. Other simulation parameters are: load of 2 N and 10 N, sliding velocity 20 mm/s. Assign the friction coefficient under water lubrication to the simulation model. For $ZrO_2$, the friction coefficients under 2 N and 10 N loads are 0.23 and 0.16, respectively. The friction coefficient between stainless steel and high entropy alloy is 0.18 at the load of 10 N.

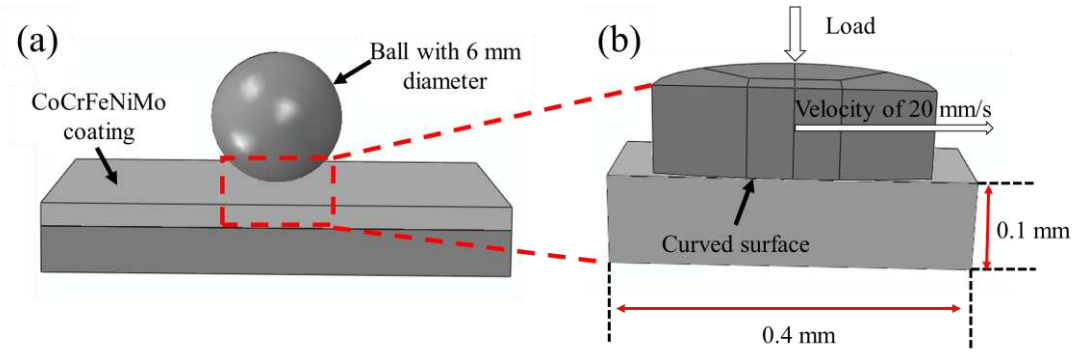


Figure 2 The schematic diagram of the sliding test simulation, a) the schematic diagram of the sliding test, b) FEA model of contact area

Table 3 CoCrFeNiMo property parameters

| Elastic modulus | Poisson's ratio | Density | Compressive strength | Tensile strength |
|---|---|---|---|---|
| $2.49\times10^5$ MPa | 0.25 | 7850 kg/m$^3$ | 929 MPa | 1441 MPa |

## 3 Results and discussion

### 3.1 Characteristics of CoCrFeNiMo coating

Figure 3 shows the cross-section of CoCrFeNiMo coating prepared by laser cladding in this work. The cross-sectional microstructure of CoCrFeNiMo coating changed from dendrite to columnar crystal from top to bottom. The difference of microstructure is mainly determined by the ratio of temperature gradient G and solidification rate R[31]. For the coating, the value of G/R near the bottom area is greater than that of the top area. Therefore, the bottom of the coating is columnar crystal and the top of the coating is dendrites crystal. According to the results of line scan, the content of Mo at the grain boundary is higher at the bottom area. As the pre-solidified crystal, dendrite consist of a small amount of Mo due to the size of Mo atom is larger than that of Co, Cr, Fe and Ni. The excess Mo is distributed to interdendrite. According to the result of EDS, the Mo content increases from 16.7 at. % in dendrite to 21.8 at. % in interdendrite.

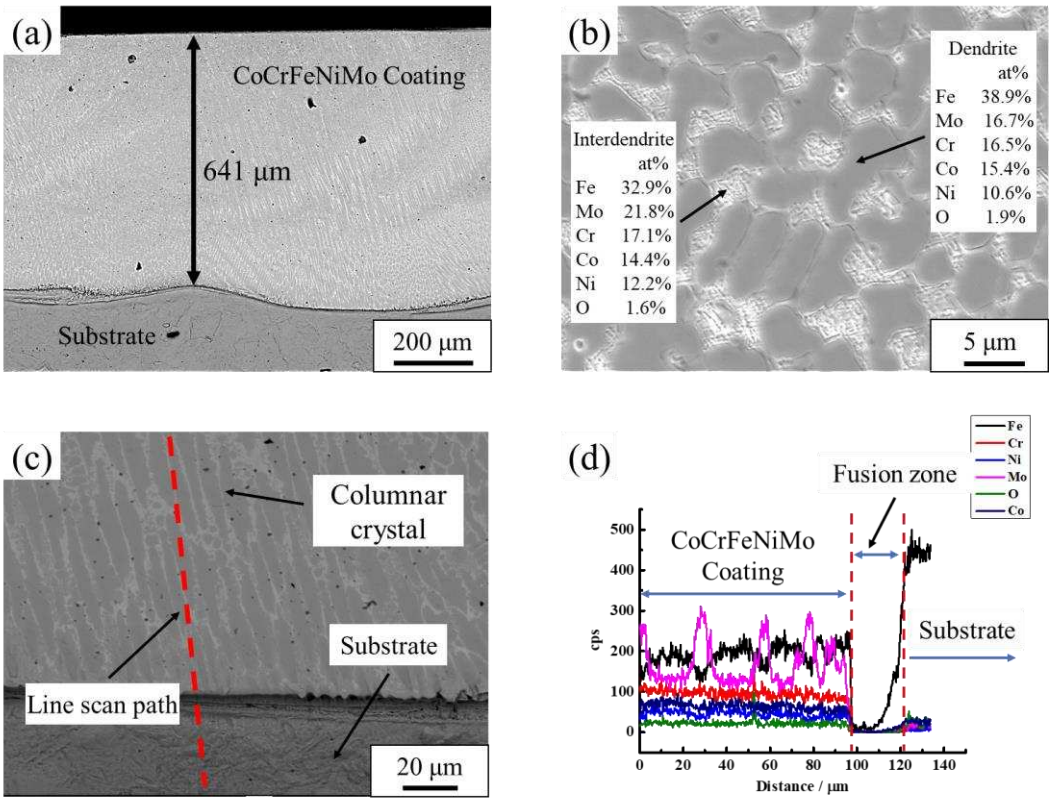


Figure 3 the cross-section of sample, a) the overall cross-section microstructure, b) the dendritic structure at the top, c) the columnar grains at the bottom, d) line scan corresponding to the red dotted line in Figure 3(c)

Figure 4 presents the XRD pattern of CoCrFeNiMo coating, and the results show that the coating mainly consists of FCC and σ phase. Precipitation strengthening improved the hardness of the CoCrFeNiMo coating due to the existence of σ phase [32]. According to Bragg's equation, the lattice constant of CoCrFeNiMo coating is 0.364 nm, while that of CoCrFeNi is only 0.359 nm[33]. The atomic size of Mo is larger than that of each elements of CoCrFeNi, increasing the lattice constant of high entropy alloy. The lattice strain caused by Mo can be calculated by the following formula[34]:

$$\varepsilon = \frac{a - a_0}{a_0} \quad (1)$$

Where $\varepsilon$ is lattice strain, $a$ is lattice constant of CoCrFeNiMo, $a_0$ is lattice constant of CoCrFeNi. The calculated result of lattice strain is 1.39%, proving the CoCrFeNiMo exhibits serious lattice distortion. Due to the serious lattice distortion, the hardness of high entropy alloy is improved, making it have good wear resistance.

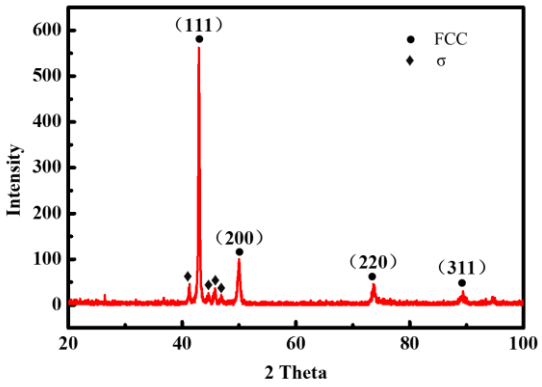


Figure 4 XRD pattern of CoCrFeNiMo HEA coatings

3.2 Potentiodynamic polarization

Figure 5 (a) and (b) present the dynamic polarization curves of CoCrFeNiMo and carburizing steel, respectively. The self-corrosion current density and self-corrosion voltage prove that the corrosion resistance of CoCrFeNiMo high entropy alloy is better than that of carburized steel. Cr, Ni, Mo, Co form their own oxidation films on the surface of CoCrFeNiMo high entropy alloy, so the dynamic polarization curve of CoCrFeNiMo has the passivation region. The passivation film can ensure that

CoCrFeNiMo will not be oxidized in water or air. Some defects are existed in the CoCrFeNiMo coating. These defects are the weak points in the passivation film, so the sudden failure of the passive film in the passivation region leads to the increase of corrosion current, forming the metastable corrosion shown in Figure 5 (a). When the $V_f$ is higher than the passive breakdown potential, rapid corrosion dissolution is occurred at the CoCrFeNiMo surface. Figure 5 (c) and (d) present the surface morphology after electrolytic corrosion. The content of Mo on the corroded surface is low, so the rapid dissolution microstructure mainly take place in interdendritic. Therefore, the corrosion resistance of dendrites is better than that of interdendritic.

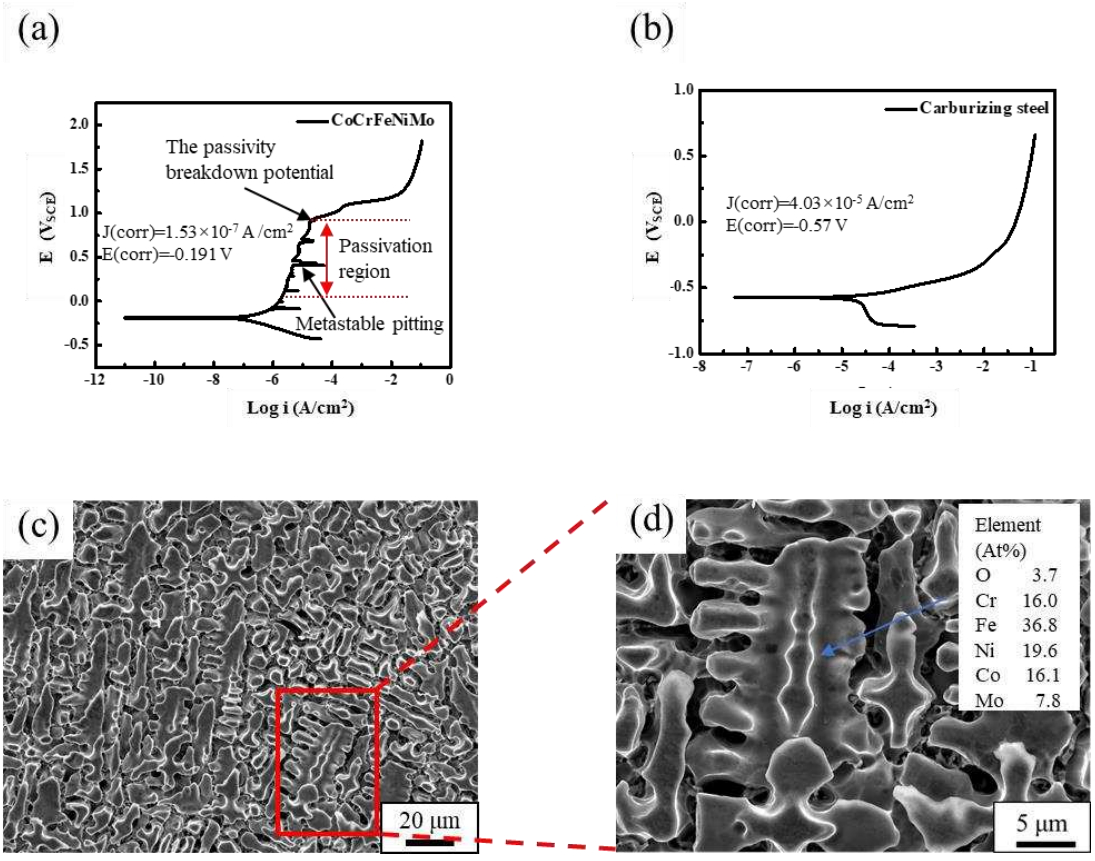


Figure 5 Potentiodynamic polarization curves and the morphology, a) CoCrFeNiMo potentiodynamic polarization curve, b) carburizing steel potentiodynamic polarization curve, c) the CoCrFeNiMo morphology after electrolytic corrosion, d) enlarged image

Figure 6 presents the XPS results of CoCrFeNiMo passive film. According to the research of stainless steel, the oxide formed by Cr contributes the most to the anti-corrosion of metal[35, 36].So, $Cr^{3+}$ in the passive film of CoCrFeNiMo mainly comes from $Cr_2O_3$ and $Cr(OH)_3$[34]. Figure 6 (b) and (d) proved that the Co-O compound, i.e.

CoO, $Co(OH)_2$ and $Co_2O_3$, and corrosion products containing Fe, i.e. FeO, $Fe_2O_3$, $Fe_3O_4$ and FeO(OH), were formed in the passive film[37, 38]. Likewise, the Ni and Mo generate NiO, $Ni(OH)_2$ and $MoO_3$, respectively[39, 40]. According to the semi-quantitative analysis of XPS, the contents of Co, Cr, Fe, Ni and Mo in the passive film were 4.0 at. %, 9.1 at. %, 8.3 at. %, 2.3 at. % and 7.0 at. %, respectively. The highest value of Cr content is obtained in the passive film, proving that Cr in CoCrFeNiMo is favor to be oxidized[41], while Ni has a low oxidation capacity due to the low Ni content in the passive film.

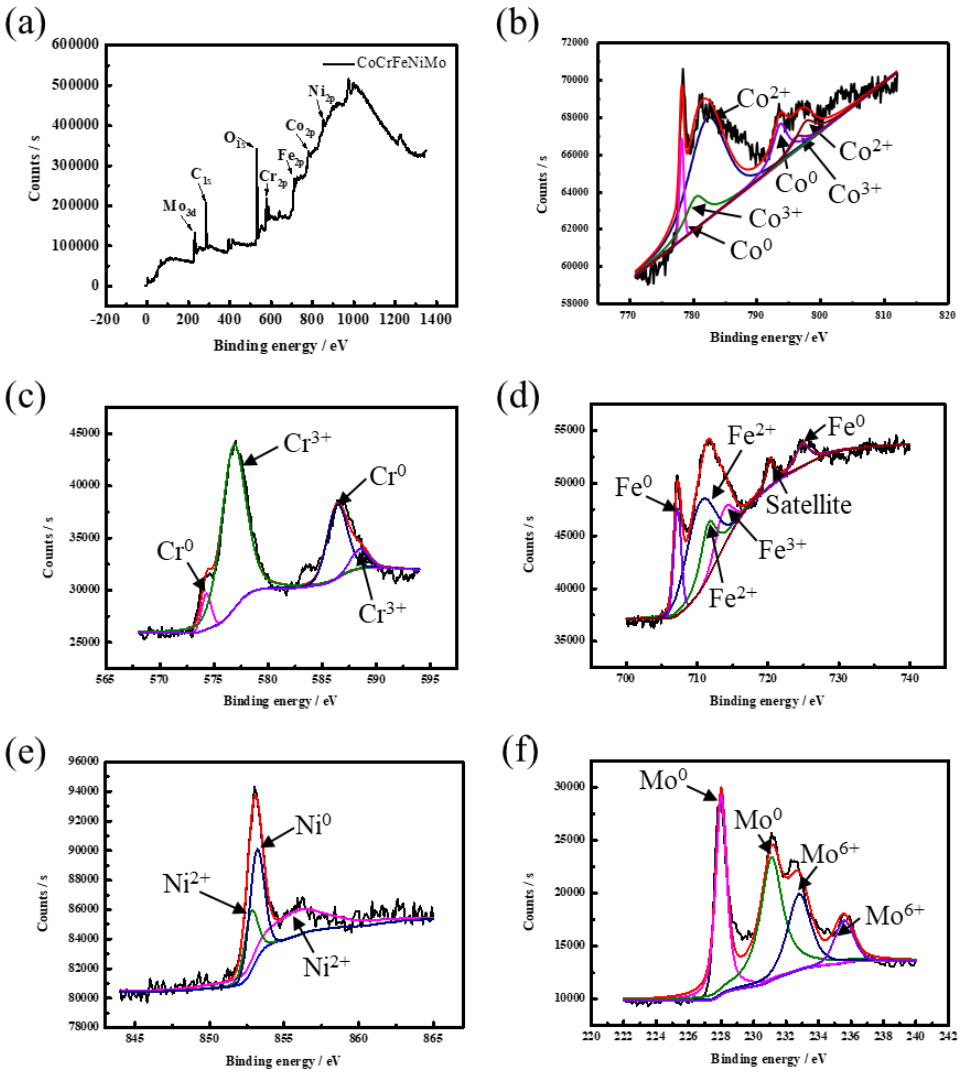


Figure 6 XPS results of CoCrFeNiMo passive film, a) full XPS spectrum, b) $Co_{2p}$, c) $Cr_{2p}$, d) $Fe_{2p}$, e) $Ni_{2p}$, f) $Mo_{3d}$

3.3 Friction and wear properties of CoCrFeNiMo HEA coating under water lubrication

The friction coefficient between CoCrFeNiMo HEA coating and $ZrO_2$/stainless steel is shown in Figure 7. For the high load shown in Figure 7(c), both $ZrO_2$ and SS ball cause high friction at running in period. However, under low load (2 N and 5 N), this phenomenon is uncertain. This phenomenon only exists in some experiments. When the load reaches a certain value, the micro convexity of the $ZrO_2$ ball surface cutted the CoCrFeNiMo surface at the beginning of sliding test, resulting in a higher friction coefficient. But for stainless steel ball, the surface of stainless-steel ball was cut by the micro convex body of CoCrFeNiMo. No obvious fluctuations of the friction coefficient were found after the running-in stage. The antifriction oxides were formed in the furrow during sliding test, causing the decrease of the friction coeffcient slightly. Figure 7 (d) illustrates that the friction coefficient decreases with the increase of load. The relative high friction coefficient value is obtained when it rubbed against stainless steel, while the relatively low value is received for $ZrO_2$. It is a common phenomenon that the friction coefficient decreases with increasing load because the formation of oxides promotes the reduction of friction coefficient.

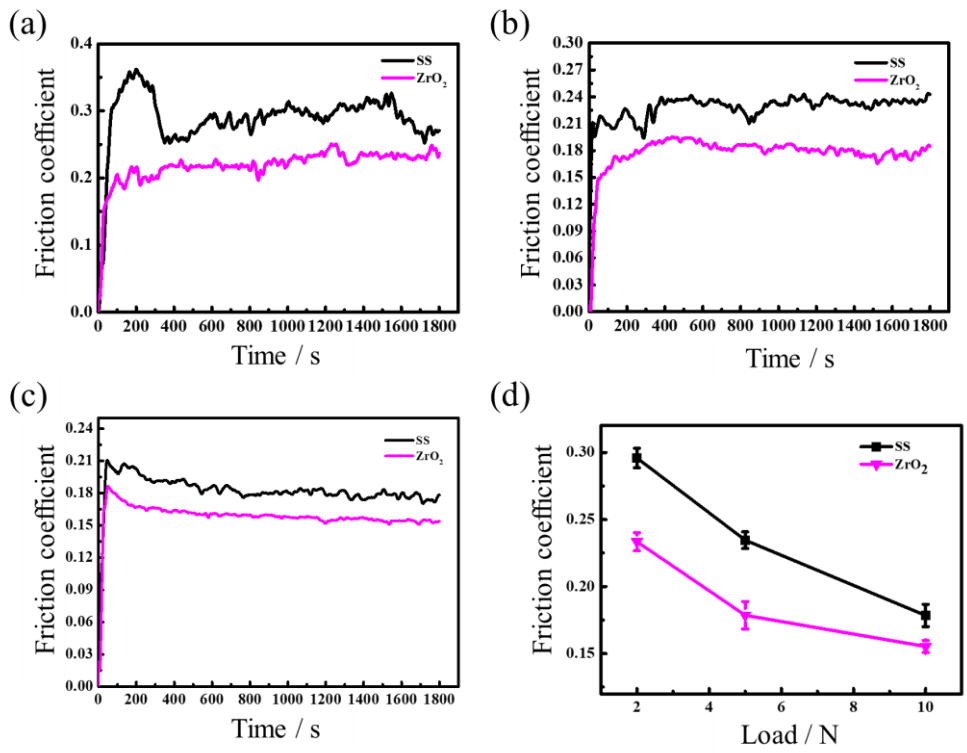


Figure 7 Friction coefficient between CoCrFeNiMo and $ZrO_2$/stainless steel (SS) ball, a) 2 N, b) 5 N, c) 10 N, d) relationship between average friction coefficient and load

The wear scar profile of CoCrFeNiMo HEA coating is shown in Figure 8. When the ball is stainless steel, the depth of the wear scar is relatively shallow, and its value ranges from 0.3 μm to 0.8 μm as the load increases from 2 N to 10 N. Because the hardness of stainless is lower than that of CoCrFeNiMo HEA coating, the wear mainly occurs on the contact surface of stainless-steel ball, resulting in the shallow wide wear mark on the CoCrFeNiMo HEA coating. Similarly, because the hardness of $ZrO_2$ is higher than that of stainless steel, the wear scar of CoCrFeNiMo slid against $ZrO_2$ are narrow and deep. As the result, wear rates of CoCrFeNiMo slid against $ZrO_2$ are higher than that of stainless steel.

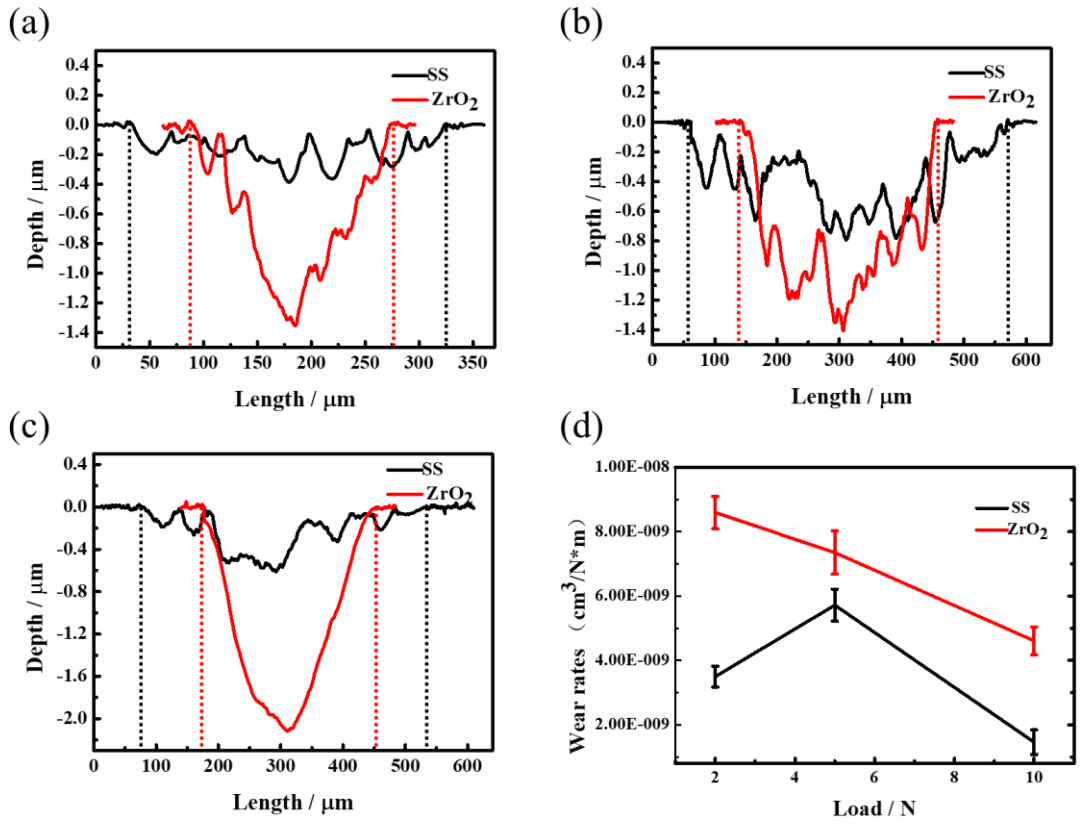


Figure 8 The cross-section profiles of worn surface of CoCrFeNiMo HEA coating slid against $ZrO_2$ and stainless steel, a) 2 N, b) 5 N, c) 10 N, d) the relationship between wear rate and load

3.4 The wear scar morphology of CoCrFeNiMo

Figure 9 shows the wear scar morphology of CoCrFeNiMo HEA slid with $ZrO_2$. The experimental results are consistent with the simulation results described below. There is no oxide film on the wear scar under 2 N load, while the wear scar under 10 N load

is covered with a layer of oxide film. In fact, there are two forms of oxide in the wear scar, one is the oxide existing in the grooves, and the other is the oxide film. Figure 9 (c) shows the oxides in the grooves. When the micro convex of $ZrO_2$ cuts the CoCrFeNiMo surface, severely plastic deformation and high flash temperature will occur in the furrow of high entropy alloy. So, the grooves contain oxides. The oxide film shown in Figure 9 (d) is caused by plastic deformation during sliding test rather than high temperature. For the ball-disk model, the approximate range of temperature rise can be estimated by the following formula[42]:

$$\theta_1 = \frac{\lambda \mu P V}{4 a \alpha J} \tag{2}$$

$$\theta_2 = \frac{0.318(1-\lambda)}{aJ}\left(\frac{V}{a\alpha\rho c}\right)^{\frac{1}{2}} \tag{3}$$

$$\frac{\lambda}{1-\lambda} = \frac{a_1/\rho_1 c_1}{a_2/\rho_2 c_2} \tag{4}$$

Where the $\theta_1$ and $\theta_2$ are the temperature of the ball and plate respectively. $\lambda$ is partition coefficient. $\mu$ is friction coefficient. $P$ and $V$ are the load and the velocity respectively. $\alpha$ is thermal conductivity. $\rho$ is the density. $a$ is the contact radius. $J$ is mechanical equivalent of heat. $c$ is specific heat. We can roughly estimate the effect of 10 N (P) load and 20 mm/s (V) on temperature rise. Take steel parameters as an example and its corresponding parameters are shown in Table 4.

Table 4. Thermal parameters of steel (mm)

| $\rho$ | $\mu$ | $c$ | $J$ | $\alpha$ |
|---|---|---|---|---|
| $7.8*10^{-9}$t/mm$^3$ | 0.5 | $0.46*10^9$ mJ/t.K | 1 | 50.2mJ/s.mm.K |

According to Figure 9 (b), the contact radius is greater than 0.1mm. Take the value into the above formula to find $\theta_1 = 2.5$ ℃, $\theta_2 = 1.6$ ℃. Even if the parameters of ceramics and high entropy alloys are different from those of steel, the temperature rise will not exceed 10 ℃.

The von Mises stress is higher than yield stress in the contact area under 10 N load (as shown in Figure 13), so more than half of the area in the wear scar is covered by oxide film. EDS result shows that the oxide film mainly contains O, Fe, Co, Cr, Ni and Mo

elements and it does not contain Zr elements, indicating that $ZrO_2$ does not participate in the reaction during oxidation.

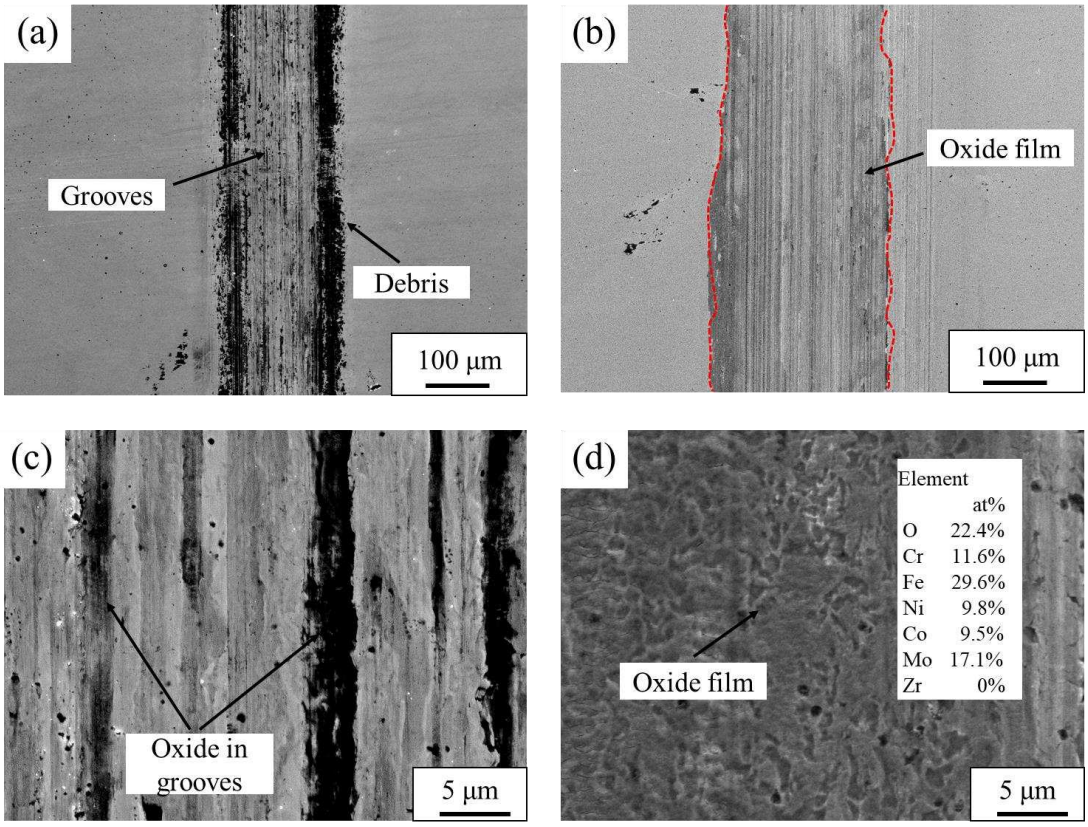


Figure 9 Wear scar of CoCrFeNiMo HEA slid with $ZrO_2$, a) wear scar at the load of 2 N, b) wear scar at the load of 10 N, c) enlarged image of oxide in grooves, d) enlarged image of oxide film

The yield strength of stainless steel is lower than CoCrFeNiMo, so when these two materials contact with each other, the stainless steel deforms first, protecting the CoCrFeNiMo from severe plastic deformation. The wear scars of CoCrFeNiMo slid with stainless steel are shown in Figure 10. The quantity of furrows and oxides decreased significantly compared with Figure 9. As the plastic deformation did not take place on the CoCrFeNiMo surface (as shown in Figure 15), no oxide film was found in the wear scar under 10 N load. The stainless steel ball only caused the destruction of the passive film on the CoCrFeNiMo surface. After the passive film of CoCrFeNiMo high entropy alloy was destroyed, the wear scar of CoCrFeNiMo shows the microstructure due to the different properties between the dendritic and interdendritic.

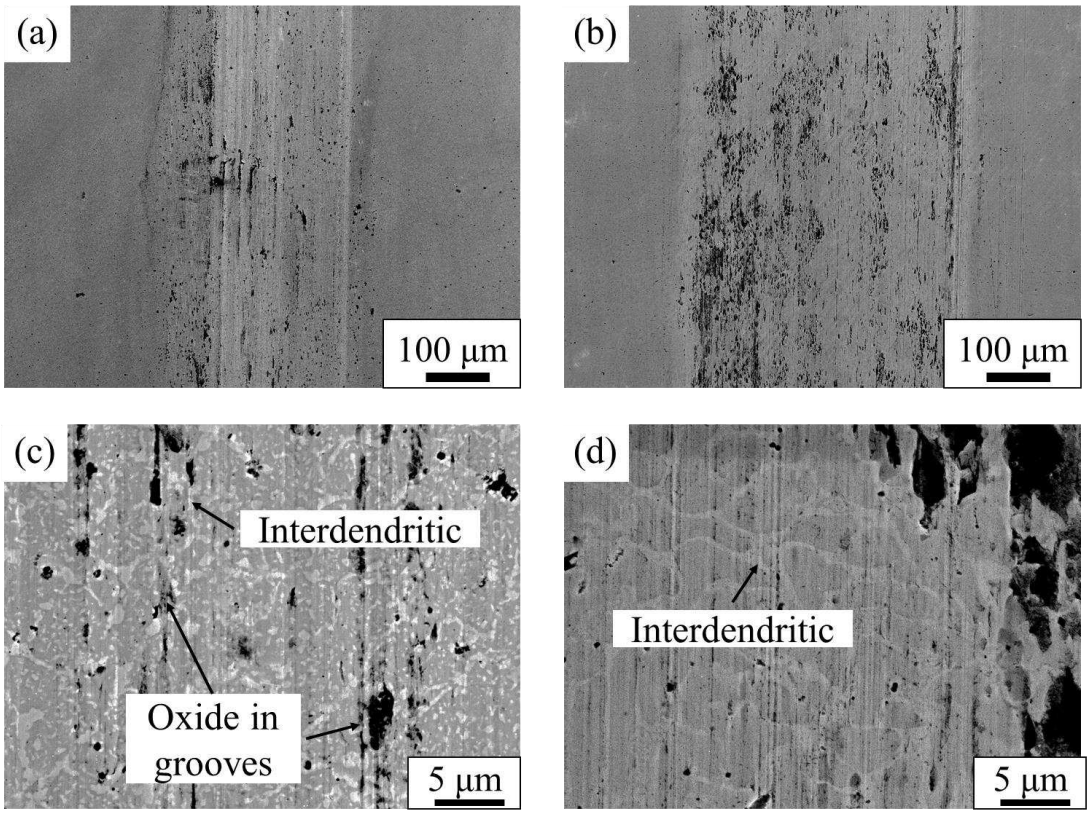


Figure 10 Wear scar of CoCrFeNiMo HEAs slid with stainless steel, a) and c) at the load of 2 N, b) and d) at the load of 10 N

Figure 11 proves that the oxide film cracked and peeled off under tensile stress. The direction of crack growth is perpendicular to the tensile stress. When the crack grew to a certain size, its propagation direction changed. With the crack propagation, the oxide film gradually separated from the matrix, and then transferred to the edge of the wear scar. Finally, the oxide film fell off and caused irregular broken trail. The oxide film shown in Figure 11 (a) is in the crack propagation stage, while Figure 11 (b) shows that the oxide film fell off and left the broken trail. These SEM images confirm the destruction of oxide film caused by cyclic tensile stress proposed (as shown in Figure 14).

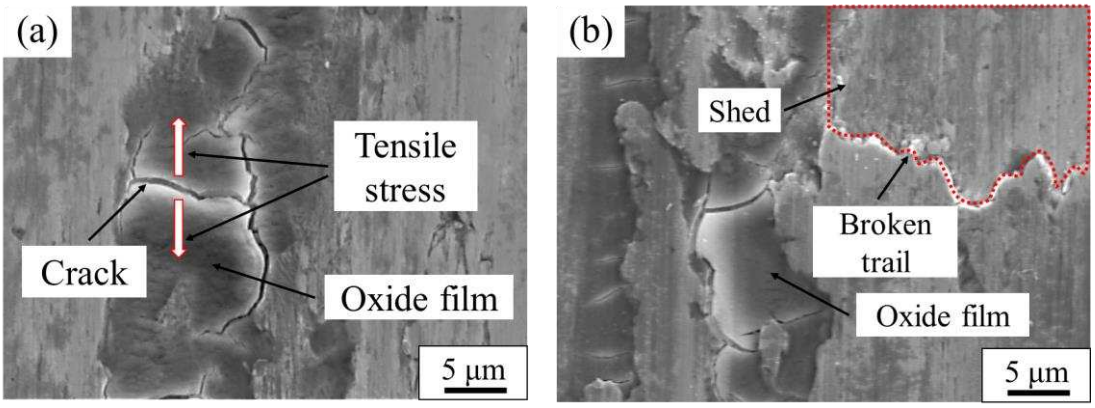


Figure 11 Cracks in oxide film at the load of 10 N, a) the oxide film cracked under tensile stress, b) the oxide films cracked and shed

Figure 12 shows the Raman spectra of oxides and oxide film in the wear scar. According to Raman results, each element in CoCrFeNiMo reacts with oxygen to form corresponding oxides. $Fe_3O_4$, $Fe_2O_3$, $MoO_3$, NiO, $Cr_2O_3$ and $Co_3O_4$ are mainly formed. Among them, $Fe_3O_4$ and $Fe_2O_3$ play a positive role in the tribological properties of CoCrFeNiMo HEA coating[43, 44], while $Cr_2O_3$ and $MoO_3$, as a kind of hard particle, can cut the CoCrFeNiMo surface to form furrows[45, 46]. According to the intensity of the peak, the oxide film contains more NiO, while the oxides in the furrow is mainly composed of $Fe_3O_4$. Figure 12 (d) shows the Raman spectrum of the high entropy alloy outside the wear scar. There is no obvious oxidation on the surface of CoCrFeNiMo outside the wear scar, because the surface passivation film protects the high entropy alloy from oxidation in water. Although oxides exist in the passivation film on the surface of high entropy alloys, the thickness of the passivation film is relatively thin and can be destroyed during Raman testing. The thickness of the oxide formed during sliding test is much larger than the thickness of passivation film, so the oxide signal can be detected in Raman test.

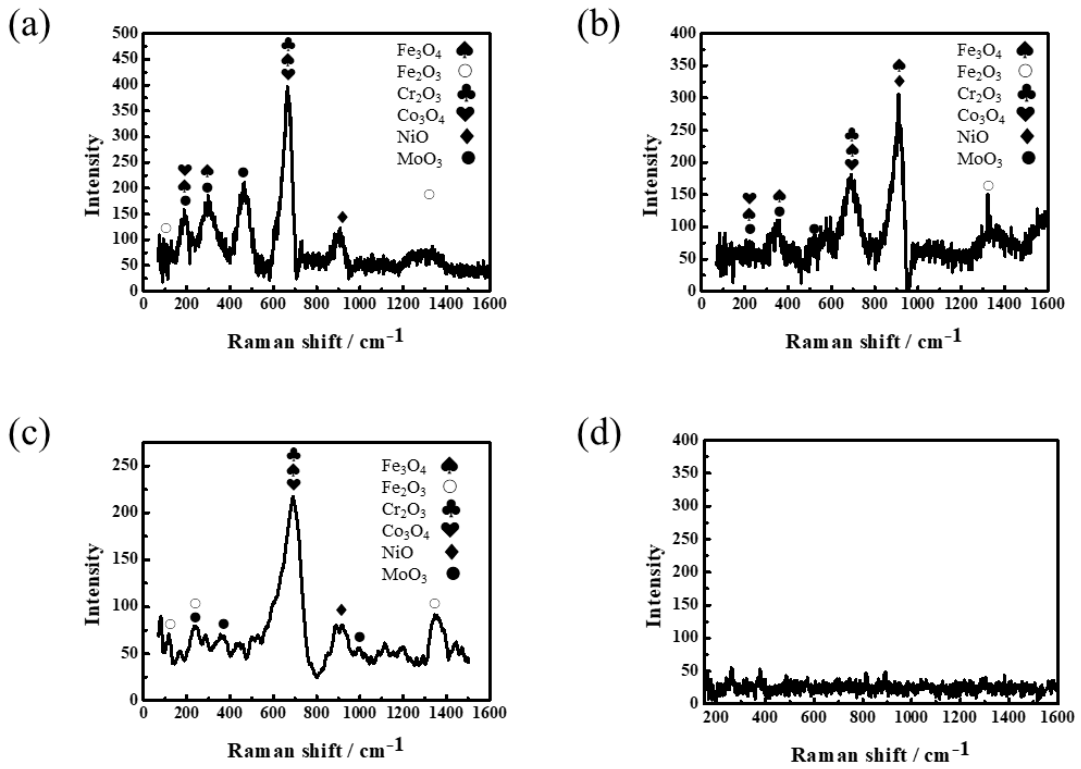


Figure 12 Raman spectra of CoCrFeNiMo HEAs surface, a) oxides in furrows when it slid with $ZrO_2$, b) oxides film in wear scar when it slid with $ZrO_2$, c) oxides in wear scar when it slid with stainless steel, d) outside the wear scar

3.5 The tribological oxide mechanism of CoCrFeNiMo high entropy alloy

Figure 13 shows the stress distribution on the CoCrFeNiMo surface when the $ZrO_2$ ball slides forward at a speed of 20 mm/s. At the load of 2 N, the maximum von Mises stress is located on the sub-surface and its value is lower than yield stress, so plastic deformation doesn't take place on the surface. However, with the load increases to 10 N, the von Mises stress of the surface and sub surface is higher than the yield strength, which means that plastic deformation take place on the surface and sub surface. The oxide film is formed in the plastic deformation area on the surface[17, 20]. According to this result, oxide film can't be formed under 2 N load, but it will be formed under 10 N load. For oxide film, fracture is related to the maximum tensile stress (the first strength theory)[47]. Figure 13 (c) and Figure 13 (d) illustrate that the surface in front of the ball is subject to compressive stress, while tensile stress is located at the surface behind the ball and its direction is parallel to the sliding direction. In general, for CoCrFeNiMo coating, the passive film in the contact area is destroyed when the ball

slides its surface. Subsequently, plastic deformation take place in this area due to high von Mises stress, resulting in the formation of oxide film. Then under the influence of periodic tensile stress, the oxide film cracks along the direction perpendicular to the tensile stress and fall off finally. But when the load is low, the surface can not form a uniform oxide film because plastic deformation doesn't take place on the surface.

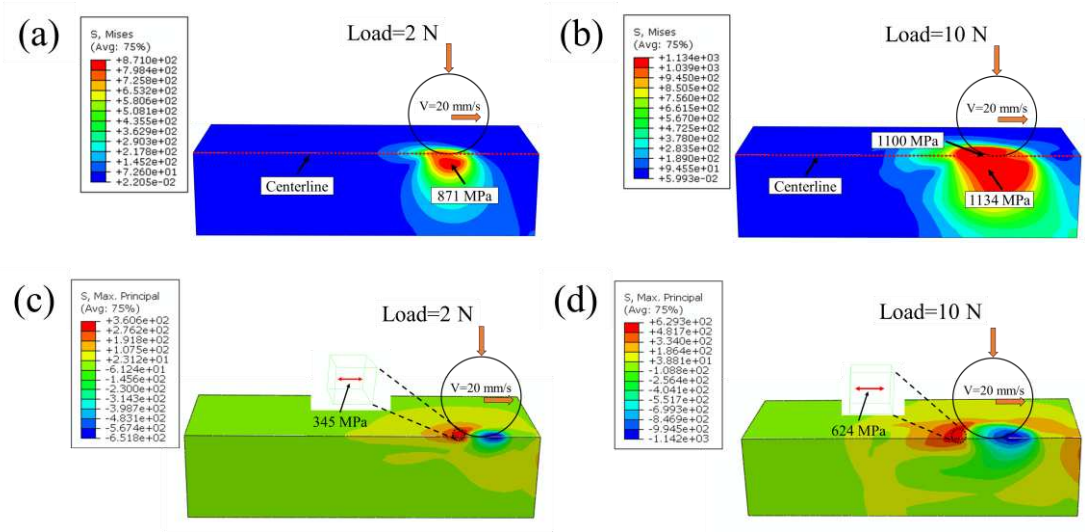


Figure 13 The stress distribution during sliding test when slid with $ZrO_2$, a) the distribution of von Mises stress (Load of 2 N, Velocity of 20 mm/s), b) the distribution of von Mises stress (Load of 10 N, Velocity of 20 mm/s), c) the distribution of maximum principle stress (MPS) (Load of 2 N, Velocity of 20 mm/s), d) the distribution of MPS (Load of 10 N, Velocity of 20 mm/s)

Figure 14 shows the contact pressure, von Mises stress and maximum principle stress distributions along the centreline (as shown in Figure 13(a)). Archard formula gives the relationship between contact stress and worn volume[48]:

$$\mathrm{V} = k\frac{Nl}{H} \tag{5}$$

Where the V is worn volume, $k$ is wear coefficient, N is normal load, $l$ is sliding distance, $H$ is the hardness. From formula (5), the differential form of wear scar depth can be derived as follows:

$$d\hbar = k\frac{P}{H}dl \tag{6}$$

Where $d\hbar$ is the incremental wear scar depth, $dl$ is the incremental sliding distance, $P$ is contact pressure. Therefore, when the ball slides on the CoCrFeNiMo surface once, the increase of the surface wear scar depth is obtained by the following formula:

$$\hbar = \int k\frac{P}{H}dl \tag{7}$$

By substituting the relevant data of Figure 8 and Figure 14 into formula 7, the wear depth of CoCrFeNiMo can be obtained when the $ZrO_2$ slides on its surface one time and its results as shown in Table 5. The passivation film is 2-14 nm[49], so it can be worn through when the ball reciprocates on the surface within 1-2 seconds. The reciprocating ball can constantly remove off the formed passivation film and expose the surface to the environment. In other words, the CoCrFeNiMo surface was not be protected by the passive film during the slide test.

The von Mises stress reaches its maximum at the edge of the contact area, so plastic deformation occurs in this area (shown in Figure 14 (b)). Von Mises stress is calculated as follows[50]:

$$\sigma_{Mises} = \sqrt{\frac{1}{2}[(\sigma_{max} - \sigma_{mid})^2 + (\sigma_{mid} - \sigma_{min})^2 + (\sigma_{min} - \sigma_{max})^2]} \tag{8}$$

Where $\sigma_{Mises}$ is von Mises stress, $\sigma_{max}$, $\sigma_{mid}$ and $\sigma_{min}$ are the maximum principal stress, the middle principal stress and the minimum principal stress respectively. When $\sigma_{mid}$ and $\sigma_{min}$ approach 0, formula (8) can be simplified as:

$$\sigma_{Mises} = \sqrt{\frac{1}{2}[(\sigma_{max} - 0)^2 + (0 - 0)^2 + (0 - \sigma_{max})^2]} = |\sigma_{max}| \tag{9}$$

Von Mises stress in some areas of the curve in Figure 14 is close to the maximum principal stress. According to Formula 9 the stress of this areas is uniaxial tensile stress due to the middle and minimum principle stress approach to 0. The oxide film formed in the plastic deformation region can crack under the cyclic tensile stress.

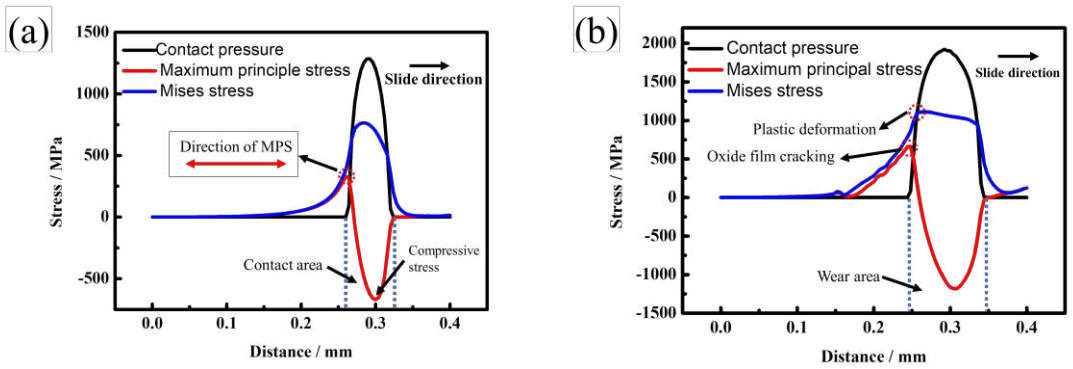


Figure 14 Contact pressure, von Mises stress and maximum principle stress distributions along the centreline when slid with $ZrO_2$, a) at the load of 2 N, b) at the load of 10 N

Table 5 the wear depth of CoCrFeNiMo when the ball slides on surface one time

| | 2 N | 10 N |
|---|---|---|
| $ZrO_2$ | 4.59 nm | 6.44 nm |
| Stainless steel | 1.94 nm | 2.04 nm |

Figure 15 shows the stress distribution and equivalent plastic strain (PEEQ) of stainless steel ball and high entropy alloy during sliding test. When the stainless steel ball contacts the high entropy alloy surface at the load of 10 N, the stainless steel ball have plastic deformation. The plastic deformation of the stainless steel ball increases the contact area and reduces the Mises stress of the high entropy alloy. Figure 15 (a) shows that the maximum Mises stress is located at the subsurface of HEA coating, and its value is 729 MPa. As shown in Figure 15 (b), only the stainless steel ball undergoes plastic deformation during the contact process, while the high entropy alloy has no plastic deformation. When the ball slides forward at a speed of 20 mm/s, the Mises stress on the sub-surface of the high entropy alloy increases to 813 MPa. At this time, there is no plastic deformation on the surface of the high entropy alloy(as shown in Figure 15 (c) and (d)). Because there is no plastic deformation on the surface of the high entropy alloy when grinding with stainless steel, no oxide film is formed in the wear scar.

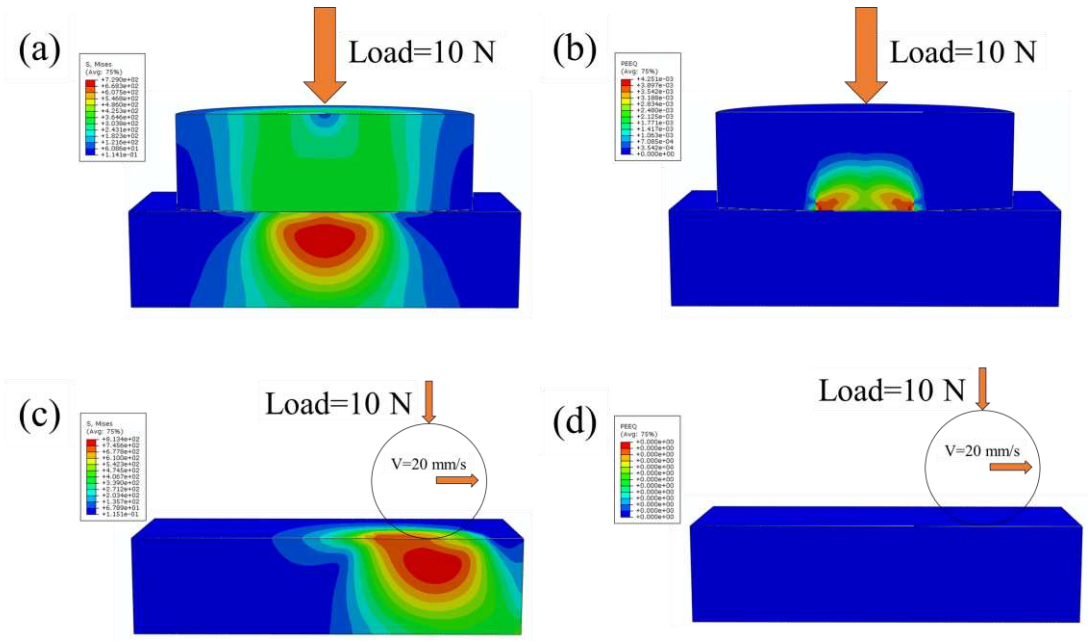


Figure 15 The stress and equivalent plastic strain (PEEQ) distribution when slid with stainless steel at the load of 10 N, a) Mises stress distribution, b) The PEEQ distribution, c) Mises stress distribution (Velocity of 20 mm/s), d) The PEEQ distribution (Velocity of 20 mm/s)

## 4 Conclusions

The tribological oxidation mechanism of CoCrFeNiMo high entropy alloy has been revealed. Contact stress, von Mises stress and tensile stress play different roles in the formation and destruction of oxide film. The key conclusions are:

(1) The passive film is formed on the CoCrFeNiMo coating surface, which is composed of $Cr_2O_3$, $Cr(OH)_3$, CoO, $Co(OH)_2$, $Co_2O_3$, FeO, $Fe_2O_3$, $Fe_3O_4$, FeO(OH), NiO, $Ni(OH)_2$ and $MoO_3$. However, because of the contact stress, the passive film was destroyed within two seconds during the sliding test.

(2) When the load increases to a certain value, the von Mises stress on the surface is higher than the yield strength of CoCrFeNiMo, causing plastic deformation. Oxide films are formed in the plastic deformation area. The above theory is proved by the oxide film produced when CoCrFeNiMo rubs with $ZrO_2$ ball under 10 N load.

(3) CoCrFeNiMo high entropy alloy slide against stainless steel proved that if the plastic deformation does not take place on the surface, no oxide film will be formed.

(4) Along the sliding direction, the front of the ball is subject to compressive stress, and

the rear of the ball is subject to tensile stress. The oxide film crack and fall off are related to cyclic tensile stress.

**Acknowledgements**

This work was financially supported by the National Natural Science Foundation of China (No. 51771228), the Fundamental Research Funds for the Central Universities, China (No. 20CX05009A and No.21CX06051A), and the Natural Science Foundation of Shandong Province (ZR2022QE073).

**Reference**

[1] C.R. LaRosa, M. Shih, C. Varvenne, M. Ghazisaeidi, Solid solution strengthening theories of high-entropy alloys, Materials Characterization 151 (2019) 310-317.
[2] Y. Zhang, T.T. Zuo, Z. Tang, M.C. Gao, K.A. Dahmen, P.K. Liaw, Z.P. Lu, Microstructures and properties of high-entropy alloys, Progress in Materials Science 61 (2014) 1-93.
[3] V.M. Gopinath, S. Arulvel, A review on the steels, alloys/high entropy alloys, composites and coatings used in high temperature wear applications, Materials Today: Proceedings 43 (2021) 817-823.
[4] J.-l. Zhou, Y.-h. Cheng, Y.-x. Chen, X.-b. Liang, Composition design and preparation process of refractory high-entropy alloys: A review, International Journal of Refractory Metals and Hard Materials 105 (2022) 105836.
[5] L. Zhicheng, K. Dejun, Structural and electrochemical corrosion properties of plasma-sprayed CoCrFeNiMo HEA coating in corrosive solutions, Corrosion Engineering, Science and Technology (2022) 1-10.
[6] S. Shuang, Z.Y. Ding, D. Chung, S.Q. Shi, Y. Yang, Corrosion resistant nanostructured eutectic high entropy alloy, Corrosion Science 164 (2020) 108315.
[7] Y.Y.B.L.P.K.T.I.C.-R.H.-E.A.A.R. Shi, Metals, 2017.
[8] P. Zhang, Z. Li, H. Liu, Y. Zhang, H. Li, C. Shi, P. Liu, D. Yan, Recent progress on the microstructure and properties of high entropy alloy coatings prepared by laser processing technology: A review, Journal of Manufacturing Processes 76 (2022) 397-411.
[9] A. Ostovari Moghaddam, N.A. Shaburova, M.N. Samodurova, A. Abdollahzadeh, E.A. Trofimov, Additive manufacturing of high entropy alloys: A practical review, Journal of Materials Science & Technology 77 (2021) 131-162.
[10] W. Li, D. Xie, D. Li, Y. Zhang, Y. Gao, P.K. Liaw, Mechanical behavior of high-entropy alloys, Progress in Materials Science 118 (2021) 100777.
[11] Z.U. Arif, M.Y. Khalid, A. Al Rashid, E. ur Rehman, M. Atif, Laser deposition of high-entropy alloys: A comprehensive review, Optics & Laser Technology 145 (2022) 107447.
[12] B. Jin, N. Zhang, H. Yu, D. Hao, Y. Ma, AlxCoCrFeNiSi high entropy alloy coatings with high microhardness and improved wear resistance, Surface and Coatings Technology 402 (2020) 126328.
[13] S.A. Firstov, V.F. Gorban', N.A. Krapivka, M.V. Karpets, A.D. Kostenko, Wear Resistance of High-Entropy Alloys, Powder Metallurgy and Metal Ceramics 56(3) (2017) 158-164.
[14] Z.-S. Nong, Y.-N. Lei, J.-C. Zhu, Wear and oxidation resistances of AlCrFeNiTi-based high

entropy alloys, Intermetallics 101 (2018) 144-151.
[15] M.-H. Chuang, M.-H. Tsai, W.-R. Wang, S.-J. Lin, J.-W. Yeh, Microstructure and wear behavior of AlxCo1.5CrFeNi1.5Tiy high-entropy alloys, Acta Materialia 59(16) (2011) 6308-6317.
[16] J.L. Mo, M.H. Zhu, Tribological oxidation behaviour of PVD hard coatings, Tribology International 42(11) (2009) 1758-1764.
[17] G. Jin, Z. Cai, Y. Guan, X. Cui, Z. Liu, Y. Li, M. Dong, D. zhang, High temperature wear performance of laser-cladded FeNiCoAlCu high-entropy alloy coating, Applied Surface Science 445 (2018) 113-122.
[18] J.-M. Wu, S.-J. Lin, J.-W. Yeh, S.-K. Chen, Y.-S. Huang, H.-C. Chen, Adhesive wear behavior of AlxCoCrCuFeNi high-entropy alloys as a function of aluminum content, Wear 261(5) (2006) 513-519.
[19] X. Pei, Y. Du, X. Hao, H. Wang, Q. Zhou, H. Wu, H. Wang, Microstructure and tribological properties of TiZrV0.5Nb0.5Alx refractory high entropy alloys at elevated temperature, Wear 488-489 (2022) 204166.
[20] X. Liu, F. Lv, H. Li, Y. Wang, X. Lu, D. Zhao, Microstructure and High-Temperature Tribological Behavior of Plasma-Sprayed FeCoCrAlNi High Entropy Alloy Coatings Under Higher Load Condition, Journal of Thermal Spray Technology 31(4) (2022) 1276-1284.
[21] Z. Guo, A. Zhang, J. Han, J. Meng, Microstructure, mechanical and tribological properties of CoCrFeNiMn high entropy alloy matrix composites with addition of Cr3C2, Tribology International 151 (2020) 106436.
[22] L.M. Du, L.W. Lan, S. Zhu, H.J. Yang, X.H. Shi, P.K. Liaw, J.W. Qiao, Effects of temperature on the tribological behavior of Al0.25CoCrFeNi high-entropy alloy, Journal of Materials Science & Technology 35(5) (2019) 917-925.
[23] C. Jin, X. Li, H. Li, Q. Li, H. Wang, Tribological performance of a TiZrNbMo0.6 refractory high entropy alloy at elevated temperatures, Journal of Alloys and Compounds 920 (2022) 165915.
[24] Y. Yu, F. He, Z. Qiao, Z. Wang, W. Liu, J. Yang, Effects of temperature and microstructure on the triblogical properties of CoCrFeNiNbx eutectic high entropy alloys, Journal of Alloys and Compounds 775 (2019) 1376-1385.
[25] G. Deng, A.K. Tieu, X. Lan, L. Su, L. Wang, Q. Zhu, H. Zhu, Effects of normal load and velocity on the dry sliding tribological behaviour of CoCrFeNiMo0.2 high entropy alloy, Tribology International 144 (2020) 106116.
[26] X. You, J. Song, P. Lin, X. Zhang, Y. Su, H. Wang, Y. Zhang, L. Hu, Tribological properties and wear mechanisms of TixVNbTaWy RHEAs sliding against Si3N4 ceramic balls: The effects of Ti and W contents, Tribology International 175 (2022) 107801.
[27] Z. Hu, W. Lu, M.D. Thouless, J.R. Barber, Effect of plastic deformation on the evolution of wear and local stress fields in fretting, International Journal of Solids and Structures 82 (2016) 1-8.
[28] L. Feng, J. Xu, The role of plastic anisotropy deformation in fretting wear predictions, Wear 260(11) (2006) 1274-1284.
[29] A. Bastola, D. Stewart, D. Dini, Three-dimensional finite element simulation and experimental validation of sliding wear, Wear 504-505 (2022) 204402.
[30] T.-T. Shun, L.-Y. Chang, M.-H. Shiu, Microstructure and mechanical properties of multiprincipal component CoCrFeNiMox alloys, Materials Characterization 70 (2012) 63-67.
[31] F. Ye, Z. Jiao, Y. Yuan, Precipitation behaviors and properties of micro-beam plasma arc cladded CoCrFeMnNi high-entropy alloy at elevated temperatures, Materials Chemistry and Physics 236 (2019) 121801.

[32] X. Gao, T. Liu, X. Zhang, H. Fang, G. Qin, R. Chen, Precipitation phase and twins strengthening behaviors of as-cast non-equiatomic CoCrFeNiMo high entropy alloys, Journal of Alloys and Compounds 918 (2022) 165584.
[33] M.A. Hassan, I.M. Ghayad, A.S.A. Mohamed, A.E. El-Nikhaily, O.A. Elkady, Improvement ductility and corrosion resistance of CoCrFeNi and AlCoCrFeNi HEAs by electroless copper technique, Journal of Materials Research and Technology 13 (2021) 463-485.
[34] S. Alleg, S. Kartout, M. Ibrir, S. Azzaza, N.E. Fenineche, J.J. Suñol, Magnetic, structural and thermal properties of the Finemet-type powders prepared by mechanical alloying, Journal of Physics and Chemistry of Solids 74(4) (2013) 550-557.
[35] R.C. Newman, M. Foong Tuck, K. Sieradzki, Validation of a percolation model for passivation of Fe-Cr alloys: I current efficiency in the incompletely passivated state, Corrosion Science 28(5) (1988) 523-527.
[36] P. Marcus, J.M. Grimal, The anodic dissolution and passivation of NiCrFe alloys studied by ESCA, Corrosion Science 33(5) (1992) 805-814.
[37] M. Smyrnioti, T. Ioannides, Synthesis of Cobalt-Based Nanomaterials from Organic Precursors.
[38] A. Rajan, M. Sharma, N.K. Sahu, Assessing magnetic and inductive thermal properties of various surfactants functionalised Fe3O4 nanoparticles for hyperthermia, Scientific Reports 10(1) (2020) 15045.
[39] A. Tarditi, M. Barroso, A. Galetti, L. Arrúa, L. Cornaglia, M. Abello, XPS study of the surface properties and Ni particle size determination of Ni supported catalysts, Surface and Interface Analysis 46 (2014).
[40] D. Su, X. Zhang, A. Wu, H. Yan, Z. Liu, L. Wang, C. Tian, H. Fu, CoO-Mo2N hollow heterostructure for high-efficiency electrocatalytic hydrogen evolution reaction, NPG Asia Materials 11(1) (2019) 78.
[41] Y. Fu, J. Li, H. Luo, C. Du, X. Li, Recent advances on environmental corrosion behavior and mechanism of high-entropy alloys, Journal of Materials Science & Technology 80 (2021) 217-233.
[42] J. Halling, Principles of Tribology, Principles of Tribology1978.
[43] X. Li, Q. Zhou, Y. Huang, J. Yang, Nanoindentation and abrasion in Fe3O4/rGO reinforced epoxy electromagnetic protective coatings, Journal of Alloys and Compounds 887 (2021) 161277.
[44] B.-A. Behrens, D. Yilkiran, S. Schöler, F. Özkaya, S. Hübner, K. Möhwald, Wear investigation of selective α-Fe 2 O 3 oxide layers generated on surfaces for dry sheet metal forming, Procedia Manufacturing 15 (2018) 923-930.
[45] J. Lince, Tribological and Chemical Effects of Long Term Humid Air Exposure on Sputter-Deposited Nanocomposite MoS2 Coatings, Wear 432-433 (2019) 202935.
[46] S. Chen, Y. Su, Q. Sun, H. Fan, J. Song, L. Hu, Y. Zhang, Strong, tough and high temperature self-lubricated fibrous monolithic ceramic in Al2O3/Cr2O3 system, Tribology International 172 (2022) 107646.
[47] W. Zhu, Y. Deng, Z. Zhang, G. Tan, X. Guo, Effect of tensile stress response for oxide films on the fatigue failure behavior of anodized AA6082 alloys, Materials Science and Engineering: A 850 (2022) 143552.
[48] T. Telliskivi, Simulation of wear in a rolling–sliding contact by a semi-Winkler model and the Archard's wear law, Wear 256(7) (2004) 817-831.
[49] M. Benoit, C. Bataillon, B. Gwinner, F. Miserque, M.E. Orazem, C.M. Sánchez-Sánchez, B. Tribollet, V. Vivier, Comparison of different methods for measuring the passive film thickness on

metals, Electrochimica Acta 201 (2016) 340-347.
[50] Y.-Z. Wang, G.-Q. Li, Y.-B. Wang, Y.-F. Lyu, Simplified method to identify full von Mises stress-strain curve of structural metals, Journal of Constructional Steel Research 181 (2021) 106624.